Monthly Notices
of the
ROYAL ASTRONOMICAL SOCIETY

MNRAS **456,** 2024–2040 (2016) doi:10.1093/mnras/stv2764

Spiral eigenmodes triggered by grooves in the phase space of disc galaxies

S. De Rijcke★ and I. Voulis★

Department Physics and Astronomy, Ghent University, Krijgslaan 281, S9, B-9000 Ghent, Belgium

Accepted 2015 November 20. Received 2015 November 19; in original form 2015 October 22

ABSTRACT

We use linear perturbation theory to investigate how a groove in the phase space of a disc galaxy changes the stellar disc's stability properties. Such a groove is a narrow trough around a fixed angular momentum from which most stars have been removed, rendering part of the disc unresponsive to spiral waves. We find that a groove can dramatically alter a disc's eigenmode spectrum by giving rise to a set of vigorously growing eigenmodes. These eigenmodes are particular to the grooved disc and are absent from the original ungrooved disc's mode spectrum. We discuss the properties and possible origin of the different families of new modes. By the very nature of our technique, we prove that a narrow phase-space groove can be a source of rapidly growing spiral patterns that are true eigenmodes of the grooved disc and that no non-linear processes need to be invoked to explain their presence in *N*-body simulations of disc galaxies. Our results lend support to the idea that spiral structure can be a recurrent phenomenon, in which one generation of spiral modes alters a disc galaxy's phase space in such a way that a following generation of modes is destabilized.

Key words: galaxies: evolution – galaxies: kinematics and dynamics – galaxies: spiral.

1 INTRODUCTION

Although it is a topic with a venerable history, the study of how disc galaxies develop their beautiful spiral patterns is far from finished. Explanations for these patterns range from the large-scale, quasi-stationary density waves envisaged by Lin & Shu (1964) to the amplification of small-scale irregularities in a differentially rotating stellar disc (Goldreich & Lynden-Bell 1965; Julian & Toomre 1966), which could be caused e.g. by small density concentrations (D'Onghia, Vogelsberger & Hernquist 2013), via feedback cycles (Mark 1977; Toomre 1981).

An attractive idea for the origin of recurrent spiral patterns as genuine modes of the stellar disc has been put forwards by Sellwood & Lin (1989) and was further developed by Sellwood & Kahn (1991), using both *N*-body simulations and analytical arguments. These authors found that a spiral pattern can carve a groove at its outer Lindblad resonance, or OLR, in a simulated disc's phase space and that this groove is most likely the cause of the growth of a next generation of spiral patterns which in turn carve their own phase-space grooves, etc. This cycle can in principle continue as long as the disc remains cool enough to support coherent waves and as long as grooves are carved in responsive regions of phase space. Each subsequent generation of spirals is radially more extended than the previous one, transporting angular momentum ever further away from the galaxy centre, in accordance with the second law of thermodynamics (Lynden-Bell & Kalnajs 1972). According to this scenario, each spiral pattern has a finite lifetime but there are always spirals present in the stellar disc.

In this paper, we further investigate this hypothesis. High-resolution *N*-body simulations are computationally expensive tools to test how grooves in different locations of phase space affect a disc's stability properties. It is, moreover, difficult to prove that a spiral pattern arising in a numerical simulation is a true eigenmode of the disc. We therefore employ PYSTAB, a fast computer code developed by us that efficiently traces the eigenmodes of a given disc galaxy model using linear perturbation theory and computes their properties (density distribution, velocity field, etc.). We present PYSTAB in Section 2 and the cored exponential galaxy disc model whose eigenmodes we will determine in Section 3. In Sections 4 and 5, we determine the $m = 2$ and $m = 4$ eigenmode spectra, respectively, of grooved versions of the disc model and discuss the properties of the eigenmodes related to the presence of a groove. The effect of the shape of the phase-space groove is investigated in Section 6. We summarize our conclusions in Section 7.

2 PYSTAB: A STABILITY ANALYSIS CODE

We use PYSTAB, a PYTHON computer code, to analyse the stability of a razor-thin stellar disc with an axisymmetric or spherically symmetric central bulge and dark-matter halo. To maximize computational efficiency, PYSTAB relies on NUMPY and SCIPY[1] routines to speed up the pure PYTHON parts of the code. Moreover, we extended PYTHON with

★ E-mail: sven.derijcke@UGent.be (SDR); ilya.voulis@UGent.be (IV)

[1] http://www.scipy.org/

fast C++ modules that interface with PYTHON via the Boost PYTHON Library.[2] These modules in turn employ routines for minimization, root finding, spline interpolation and numerical quadrature from the GNU Scientific Library.[3] The routines for solving linear systems and for matrix eigendecompositions are taken from the C++ linear algebra library ARMADILLO (Sanderson 2010). The code is controlled from a Graphical User Interface (GUI), implemented in PYQT4,[4] and contains a wide variety of numerical checks on the results as well as plotting options. The mathematical formalism behind this code can be found in Dury et al. (2008) and Vauterin & Dejonghe (1996). For completeness, we summarize it below.

The halo and bulge are assumed to be dynamically too hot to develop any instabilities and enter the calculations only via their contributions to the global gravitational potential. We only consider the stellar component of the disc and neglect the dynamical influence of gas and dust. We describe an instability as the superposition of a time-independent axisymmetric equilibrium configuration and a perturbation that is sufficiently small to warrant the linearization of the Boltzmann equation. The equilibrium configuration is characterized completely by the global potential $V_0(r)$ and the distribution function, or DF, $f_0(E, J)$. Here and in the following,

$$E = V_0(r) - \frac{1}{2}\left(v_r^2 + v_\theta^2\right) \tag{1}$$

$$J = r v_\theta \tag{2}$$

are a star's binding energy and angular momentum, respectively. We use polar coordinates (r, θ) in the stellar disc, with associated radial and tangential velocity components (v_r, v_θ).

A general perturbing potential can be expanded in a series of normal modes of the form

$$V_{\rm pert}(r, \theta, t) = V_{\rm pert}(r) \mathrm{e}^{\mathrm{i}(m\theta - \omega t)}, \tag{3}$$

with multiplicity m, pattern speed $\Re(\omega)/m$ and growth rate $\Im(\omega)$, that, owing to the linearity of the relevant equations, can be studied independently from each other. We write the response of the DF to a perturbation as:

$$f(r, \theta, v_r, v_\theta, t) = f_0(E, J) + f_{\rm resp}(r, \theta, v_r, v_\theta, t). \tag{4}$$

The evolution of the perturbed part of the DF is calculated using the linearized collisionless Boltzmann equation:

$$\left.\frac{D f_{\rm resp}}{D t}\right|_0 = -\frac{\partial f_0}{\partial \boldsymbol{v}} . \nabla V_{\rm pert}. \tag{5}$$

The left-hand side of equation (5) is the total time derivative of $f_{\rm resp}$ along an orbit in the unperturbed potential V_0. If we integrate equation (5) along an unperturbed orbit, we immediately obtain the response of the DF to the perturbing potential given by equation (3):

$$f_{\rm resp}(r, \theta, v_r, v_\theta, t) = \frac{\partial f_0}{\partial E} V_{\rm pert}(r, \theta, t) + \mathrm{i}\left[\omega \frac{\partial f_0}{\partial E} - m \frac{\partial f_0}{\partial J}\right] \times \int_{-\infty}^{t} V_{\rm pert}(r(t')) \mathrm{e}^{\mathrm{i}(m\theta(t') - \omega t')} \mathrm{d}t'. \tag{6}$$

The integral in equation (6) converges if the perturbation disappears for $t \to -\infty$ and is growing sufficiently fast in time. Changing variables such that

$$t' = t + t''$$
$$\theta(t') = \theta + \theta''(t''), \tag{7}$$

this expression can be brought in the same harmonic form as the potential perturbation

$$f_{\rm resp}(r, \theta, v_r, v_\theta, t) = f_{\rm resp}(r, v_r, v_\theta) \mathrm{e}^{\mathrm{i}(m\theta - \omega t)} \tag{8}$$

with

$$f_{\rm resp}(r, v_r, v_\theta) = \frac{\partial f_0}{\partial E} V_{\rm pert}(r) + \mathrm{i}\left[\omega \frac{\partial F_0}{\partial E} + m \frac{\partial F_0}{\partial J}\right] \times \int_{-\infty}^{0} V_{\rm pert}(r(t'')) \mathrm{e}^{\mathrm{i}(m\theta''(t'') - \omega t'')} \mathrm{d}t''. \tag{9}$$

Along an unperturbed orbit, the radial coordinate r is a periodic function of time with angular frequency ω_r, just like v_r en v_θ. $\theta(t)$ is the superposition of a periodic function $\theta_p(t)$ and a uniform drift, $\omega_\theta t$:

$$\theta(t'') = \omega_\theta t'' + \theta_p(t''). \tag{10}$$

Since $\theta''(0) = 0$, it follows that $\theta_p(0) = 0$. We separate the part of the integrand in equation (6) that is periodic with frequency ω_r from the aperiodic part and expand it in a Fourier series,

$$V_{\rm pert}(r(t'')) e^{im\theta_p(t'')} = \sum_{l=-\infty}^{\infty} I_l \mathrm{e}^{\mathrm{i}l\omega_r t''}, \tag{11}$$

with purely real Fourier coefficients I_l.

Instead of using E and J, orbits in the unperturbed potential are catalogued by their apocentre and pericentre distances, denoted by $r_{\rm apo}$ and $r_{\rm peri}$, respectively. The sense of rotation is indicated by the sign of $r_{\rm peri}$. For each orbit in a 300 × 300 grid in $(r_{\rm peri}, r_{\rm apo})$-space, each passing through its apocentre at $t = 0$, we store ω_r and ω_θ and tabulate t and θ_p as a function of radius. These two offsets in time and azimuth are necessary if one wants to compute the response DF for an orbit that does not pass through its apocentre at $t = 0$. Thus, the method samples phase space on a total of 44 850 grid points. We have tested the numerical convergence of the method in terms of orbital phase-space coverage by also using 200 × 200 and 400 × 400 grids in $(r_{\rm peri}, r_{\rm apo})$-space. While there was still a noticeable difference between the mode frequencies (see below) when going from a 200 × 200 to a 300 × 300 grid, this difference was negligible when comparing the 400 × 400 and 300 × 300 grids. In the end, we settled for a 300 × 300 grid in $(r_{\rm peri}, r_{\rm apo})$-space. We checked that this grid offers sufficient resolution for all models presented in this paper.

With

$$\int_{-\infty}^{0} V_{\rm pert}(r(t'')) \mathrm{e}^{\mathrm{i}(m\theta''(t'') - \omega t'')} \mathrm{d}t'' = -\mathrm{i} \sum_l \frac{I_l}{m\omega_\theta + l\omega_r - \omega},$$
$$V_{\rm pert}(r) = V_{\rm pert}(r(t'' = 0)) = \sum_l I_l, \tag{12}$$

the response of the DF to the perturbation now assumes the following concise form:

$$f_{\rm resp}(r, v_r, v_\theta) = \sum_l I_l \left[(l\omega_r + m\omega_\theta)\frac{\partial f_0}{\partial E} - m \frac{\partial f_0}{\partial J}\right] \times \frac{\mathrm{e}^{\mathrm{i}(l\omega_r t(r) - m\theta_p(r))}}{l\omega_r + m\omega_\theta - \omega}. \tag{13}$$

From the response DF it is in principle possible to compute the response density, $\rho_{\rm resp}(r, \theta, t)$ and, via the Poisson equation, the

[2] http://www.boost.org
[3] http://www.gnu.org/software/gsl/
[4] http://www.riverbankcomputing.com/software/pyqt/

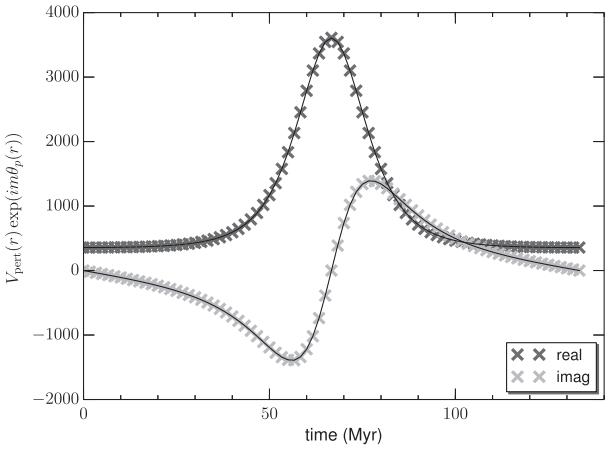

Figure 1. The actual (black lines) and Fourier-reconstructed (grey crosses) behaviour of the real and imaginary parts of the r-periodic part of a typical potential basis function V_l over one radial oscillation of an orbit.

response potential, $V_{\rm resp}(r,\,\theta,\,t)$. In order to cast the search for eigenmodes in the form of a matrix eigenvalue problem (Kalnajs 1977), we employ a family of basis density-potential pairs, $\rho_l(r)$ and $V_l(r)$. We adopt a basis set of 24 density basis functions of the form

$$\rho_l(r) = r^{m-1}\rho_0(r)\exp\left(-\frac{1}{2}\left(\frac{r-r_l}{\sigma_l}\right)^2\right) \tag{14}$$

where the average radii r_l cover the complete stellar disc and are evenly spaced on a logarithmic scale so the resolution is highest in the inner regions of the disc. The widths σ_l are automatically chosen such that the consecutive basis functions are unresolved according to the Rayleigh criterion. The radial part of any perturbation can be expanded in these basis functions:

$$V_{\rm pert}(r) = \sum_l a_l V_l(r). \tag{15}$$

We denote the response to the perturbation V_l with pattern frequency ω by $\rho_{l,{\rm resp}}(r,\,\omega)$. The Fourier coefficients of the expansion (11), for each potential basis function as perturbing potential, and for all orbits in the $(r_{\rm peri},\,r_{\rm apo})$-grid, are computed and stored. The Fourier expansion is performed from order $l=-40$ up to $l=+40$. In Fig. 1, we show the good agreement between the actual (black lines) and the Fourier-reconstructed (grey crosses) behaviour of the r-periodic part of such a perturbing potential over one radial oscillation of a typical orbit. Only the most extreme radial orbits suffer from the Gibbs phenomenon, inherent to using a finite Fourier series to reconstruct a sharply varying function. However, such orbits will be virtually free from stars in most realistic disc galaxy models.

Expanding the response $\rho_{l,{\rm resp}}(r,\,\omega)$ in the basis functions with coefficients $C_{kl}(\omega)$ yields

$$\rho_{l,{\rm resp}}(r,\,\omega) = \sum_k C_{kl}(\omega)\rho_k(r). \tag{16}$$

The coefficients $C_{kl}(\omega)$ can easily be obtained via a least-squares fit on a grid of r-values. The response to a general perturbation (15) can then be written as

$$\begin{aligned}\rho_{\rm resp}(r,\,\omega) &= \sum_l a_l \rho_{l,{\rm resp}}(r,\,\omega)\\ &= \sum_l a_l \sum_k C_{kl}(\omega)\rho_k(r).\end{aligned} \tag{17}$$

Likewise,

$$V_{\rm resp}(r,\,\omega) = \sum_l a_l \sum_k C_{kl}(\omega)V_k(r). \tag{18}$$

For an eigenmode, $V_{\rm resp} = V_{\rm pert}$, and

$$a_k = \sum_l C_{kl}(\omega)a_l \;\rightarrow\; A = C(\omega)A. \tag{19}$$

In other words, the matrix C has a unity eigenvalue for an eigenmode and the corresponding eigenvector A yields the expansion of the response density in terms of the basis functions.

Obviously, we need to be able to efficiently compute $\rho_{l,{\rm resp}}(r,\,\omega)$ for a variety of ω values. Computing a response density implies a computationally very expensive double integral of the response DF over velocity space. However, as shown by Vauterin & Dejonghe (1996), the response density $\rho_{l,{\rm resp}}(r)$ can be written as a Hilbert transform,

$$\rho_{l,{\rm resp}}(r) = \int \frac{W_l(r,\,p)}{p-\omega}{\rm d}p, \tag{20}$$

where the ω-independent functions $W_l(r,\,p)$ can be pre-computed from the response DF and stored for a grid of r and p values. Thus, the response densities $\rho_{l,{\rm resp}}(r,\,\omega)$, and hence the matrix $C(\omega)$, can be calculated efficiently for different values for ω. Thus, PYSTAB is capable of computing the eigenmode spectrum of any disc galaxy model.

3 THE CORED EXPONENTIAL DISC MODEL

The disc galaxy model introduced by Jalali & Hunter (2005) lives in a spherically symmetric soft-centred logarithmic binding potential of the form

$$V_0(r) = -\frac{v_0^2}{2}\ln\left(1+\frac{r^2}{r_c^2}\right). \tag{21}$$

Here, v_0 is the asymptotic velocity reached in the flat part of the rotation curve and r_c is a scalelength. The angular velocity, $\Omega(r)$, epicyclic frequency, $\kappa(r)$ and $m=2$ and $m=4$ Lindblad frequencies, $\Omega(r)\pm\kappa(r)/m$, are shown as a function of radius in Fig. 2. Since $\Omega(r)$ does not diverge for zero radius, it is perfectly possible for modes to have no corotation resonance, or CR.

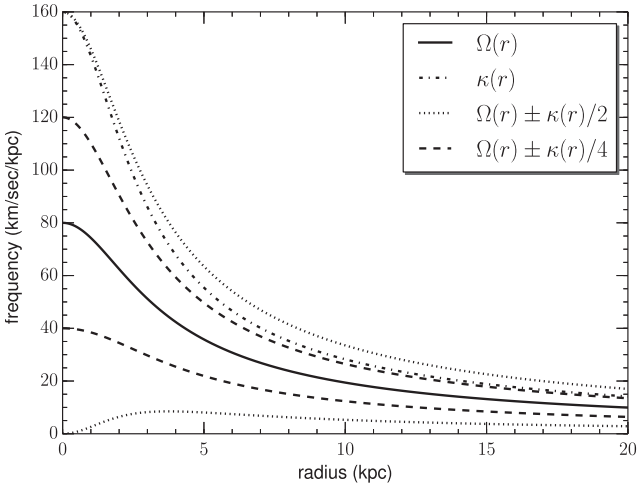

Figure 2. The angular velocity, $\Omega(r)$, epicyclic frequency, $\kappa(r)$ and $m=2$ and $m=4$ Lindblad frequencies, $\Omega(r)\pm\kappa(r)/m$, of the cored exponential disc model with a logarithmic potential.

The quasi-exponential stellar surface density of the razor-thin responsive disc is

$$\rho_0(r) = \rho_s \exp\left(-\lambda\sqrt{1+\frac{r^2}{r_c^2}}\right) \tag{22}$$

with $\rho_s = e^{\lambda}\rho_0(0)$ and $\lambda = r_c/r_D$ with r_D the scalelength of the exponential disc. The DF that self-consistently generates the surface density (22) within the binding potential (21) is given by

$$\begin{aligned} f_0(E,J) &= \rho_s \sum_{n=0}^{N} \binom{N}{n} \left(\frac{J}{r_c}\right)^{2n} g_n(E), \qquad J > 0 \\ &= 0 \qquad\qquad\qquad\qquad\qquad\qquad J \le 0 \end{aligned} \tag{23}$$

with

$$\begin{aligned} g_n(E) = &\frac{1}{2^n\sqrt{\pi}\Gamma\left(n+\frac{1}{2}\right)} \\ &\times \frac{d^{n+1}}{dE^{n+1}}\left[\exp\left(2N\frac{E}{v_0^2} - \lambda\exp\left(-\frac{E}{v_0^2}\right)\right)\right]. \end{aligned} \tag{24}$$

This DF is smoothly tapered to zero at $J = 0$ by multiplying it with a cutout function of the form

$$H_{\rm cut}(J) = 1 - \exp\left(-\frac{J^2}{J_0^2}\right). \tag{25}$$

This obviously removes stars close to the galaxy centre, causing a central hole in the stellar surface density. The DF of this disc galaxy model in turning-point space is plotted in the top panel of Fig. 3. This DF is clearly weighted towards quasi-circular orbits (the diagonal line in this diagram) and contains very few stars on radial orbits (the vertical axis of the diagram). We also smoothly taper the stellar density to zero at an outer radius of 25 kpc. Here, we choose the following values for all parameters involved:

$$\begin{aligned} N &= 6 \\ v_0 &= 200\ {\rm km\ s^{-1}} \\ r_c &= r_D = 2.5\ {\rm kpc} \rightarrow \lambda = 1 \\ J_0 &= 50\ {\rm kpc\ km\ s^{-1}} \\ \rho_s &= 0.42\frac{v_0^2}{Gr_c} = 1.56\times10^9\ {\rm M_\odot\ kpc^{-2}}. \end{aligned} \tag{26}$$

We choose $r_c = r_D$ to be able to compare the mode analysis of the cored exponential disc presented here with the analyses done by Jalali & Hunter (2005), Jalali (2007) and Omurkanov & Polyachenko (2014). We show the stellar kinematics of this model, computed numerically as velocity moments of the DF, in Fig. 3.

In Fig. 4, we show the $m = 2$ mode spectrum of this exponential disc model in the complex frequency plane. The grey-scale traces the value of $\min(|\lambda - 1|)$: the smallest distance between 1 and any of the eigenvalues of $C(\omega)$. For eigenmodes, this distance is zero (dark regions); they are indicated with white dots in Fig. 4. The triangular data points mark the position of the eigenmodes as found by Omurkanov & Polyachenko (2014) using different methods. Dots with the same tint are different frequency estimates for the same eigenmode; their spread gives an indication on the intrinsic uncertainty on the eigenmode frequencies. No growing modes exist with pattern speeds low enough to have an inner Lindblad resonance, or ILR. The sequence of growing modes ends with a neutral mode at $\omega_{\rm real} \approx 32$ km s^{-1} kpc^{-1}, well above the limit $\omega_{\rm real} = 17.0$ km s^{-1} kpc^{-1} for having an ILR (cf. Fig. 2).

Omurkanov & Polyachenko (2014) investigated the stability properties of this disc galaxy model using the linear matrix method

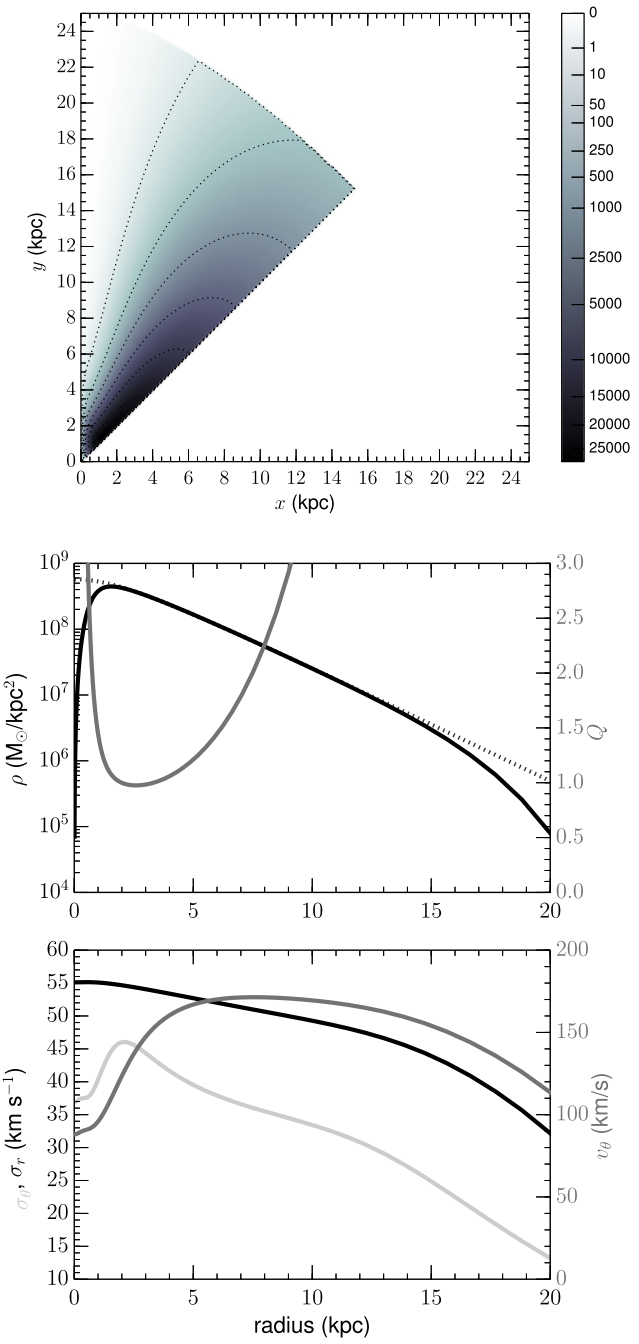

Figure 3. Top panel: the distribution function of the cored exponential disc model with a central cutout, shown in turning-point space. The colour bar indicates the phase-space density expressed in $\rm M_\odot\ kpc^{-2}\ (km\ s^{-1})^{-2}$. Middle panel: the stellar density, ρ (black curve, left axis) and the Toomre Q-parameter (dark grey curve, right axis). The dotted black curve traces the stellar density (22), without inner cutout and outer tapering. Bottom panel: the radial velocity dispersion, σ_r (black curve, left axis), tangential velocity dispersion, σ_θ (light grey curve, left axis) and the mean rotation velocity, v_θ (dark grey curve, right axis) of the cored exponential disc model with an inner cutout.

(PME) of Polyachenko (2005), the linear method using basis function (ECB) of Jalali (2007) and the finite element method (FEM) of Jalali (2010), both in its full form (FEMf) and in its restricted form suitable for models dominated by quasi-circular orbits (FEMc). Contrary to PYSTAB, which uses polar coordinates throughout, these

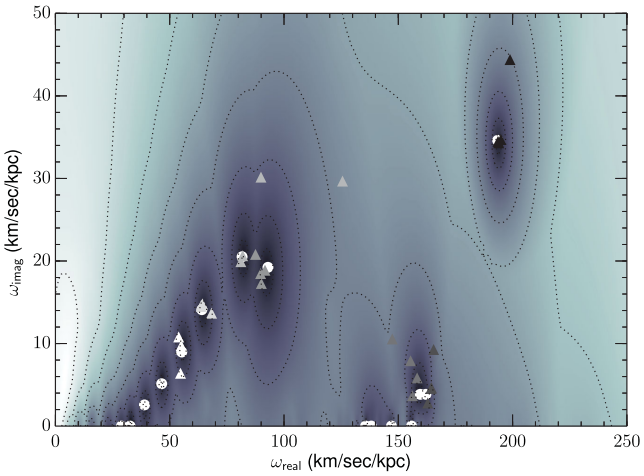

Figure 4. The mode spectrum of the cored exponential disc model (Jalali & Hunter 2005) in the complex frequency plane. The white dots indicate the location of the eigenmodes, in the centres of the dark-hued regions, as found with PYSTAB. The triangular data points mark the position of the fastest rotating eigenmodes as found by Omurkanov & Polyachenko (2014) using different methods. Dots with the same tint are different frequency estimates for the same eigenmode.

methods all employ action-angle variables in phase space. They all rely on a Fourier expansion of the perturbing potential, truncated at some order and the integration of a finite number of orbits. The PME method, as used in Omurkanov & Polyachenko (2014), uses 10 Fourier terms and 1000 orbits. The ECB method uses an expansion of the response DF and potential in a basis of 15 rather contrived trial functions of the action variables. For the FEM method, the disc is divided in N rings in which the response potential is expanded in N_d basis functions. Here, $N = 100$ and $N_d = 2$. The ECB results reported in Jalali (2007) were obtained using 10 Fourier terms and 15 trial functions.

Overall, the agreement between PYSTAB and these other mode analysis methods is very satisfactory. We list the frequencies of the retrieved eigenmodes, together with their names as given by Jalali (2007), in Table 1. The surface density perturbation of the nine most prominent $m = 2$ eigenmodes of the cored exponential disc model, as named by Jalali (2007), is presented in Fig. 5. These density plots can be directly compared with figs 3 and 4 in Omurkanov & Polyachenko (2014). Overall, the agreement is satisfactory in terms of size, shape and number of density enhancements along the arms. This code comparison makes us confident that PYSTAB works properly and that the results are reliable. As a final test of the

Table 1. Real and imaginary parts of the frequencies of the fastest growing modes of the cored exponential disc model with a central cutout. The naming of the modes is taken from Jalali (2007).

Name	ω_{real} (km s^{-1} kpc^{-1})	ω_{imag} (km s^{-1} kpc^{-1})
B1	193.91	34.50
C2	162.51	4.41
C1	158.94	4.81
B2	92.35	19.25
S1	82.18	20.88
S2	64.53	14.34
S3	55.76	10.11
S4	46.39	5.90
S5	38.97	2.88

formalism, we compute the torque exerted by the spiral pattern on the stellar disc. As shown by Zhang (1996, 1998), the torque $d\tau_z(r)$ on an annular ring of stars with radius r and width dr is given by

$$d\tau_z(r) = r dr \int_0^{2\pi} \rho_{resp} \frac{\partial V_{resp}}{\partial \theta} d\theta = -\frac{m}{2} \tilde{\rho}_{resp}(r) \tilde{V}_{resp}(r) \sin(m\gamma_0(r)) dr. \quad (27)$$

Here, $\tilde{\rho}_{resp}$ and $\tilde{V}_{resp}$ are the real amplitudes of the spiral density and binding potential and γ_0 is the phase shift between the pattern potential and density. If $d\tau_z$ is negative, the stars lose angular momentum to the spiral pattern; otherwise, they gain angular momentum from the pattern. For a pattern with a negligible radial amplitude variation, the transition from angular momentum loss to angular momentum gain should occur precisely at the CR radius although this is at best an approximation. Since no external forces act on the stellar disc, the total torque $\tau_z = \int_0^\infty d\tau_z(r)$ should be exactly zero (Polyachenko & Just 2015).

In Fig. 6, $d\tau_z(r)$ and $\tau_z(r) = \int_0^r d\tau_z$ are shown for three representative eigenmodes of the cored exponential disc model: B1, B2 and S3. $d\tau_z(r)$ is negative at small radius, changes sign at about two-thirds of the CR radius (if there is a CR) and is positive at large radii. Hence, the cumulative torque $\tau_z(r)$ first becomes zero and then rises again to zero at large radii. Clearly, the formalism presented here conserves the total angular momentum of the stellar disc with excellent precision: the asymptotic value of τ_z was found to be always smaller than $\sim 10^{-4}$ times its extreme value.

4 GROOVES AND m=2 MODES

Sellwood & Lin (1989) have reported on the occurrence of successive generations of spiral patterns in numerical simulations of stellar discs. As the inner disc gets steadily dynamically warmer, each generation of patterns decays and a new one grows but with lower pattern speeds and larger radial extent than the previous one. These authors argue that the dominant member of one particular generation of patterns is a true eigenmode of the stellar disc as it is at that time but not of the original disc. Therefore, the dynamical changes wrought by the previous generation of patterns are instrumental in triggering the next one. A detailed analysis of the evolution of stars in phase space has led Sellwood & Lin (1989) to propose the following cyclical mechanism for recurrent spiral modes:

(i) a depopulated narrow groove at a location in phase space to which the disc is very responsive causes a set of modes to grow
(ii) when each mode saturates and finally decays, it transports its angular momentum to its OLR, pushing stars there towards higher angular momenta, thus creating new phase-space grooves
(iii) the grooves that fall in a responsive part of phase space cause a new set of modes to grow

As long as the stellar disc can be cooled, e.g. by star formation, this cycle can in principle continue. One caveat is that each successive generation of spiral modes is spatially more extended than the previous one and that the grooves can end up in unresponsive parts of phase space and therefore produce no new modes, thus halting the cycle. At least in this particular case, the disc is unresponsive to the high-J_{groove} grooves that are expected from later generations of spiral patterns.

In order to investigate how a narrow groove in phase space affects the stability properties of a stellar disc, we adopt the cored exponential model from the previous paragraph and remove stars

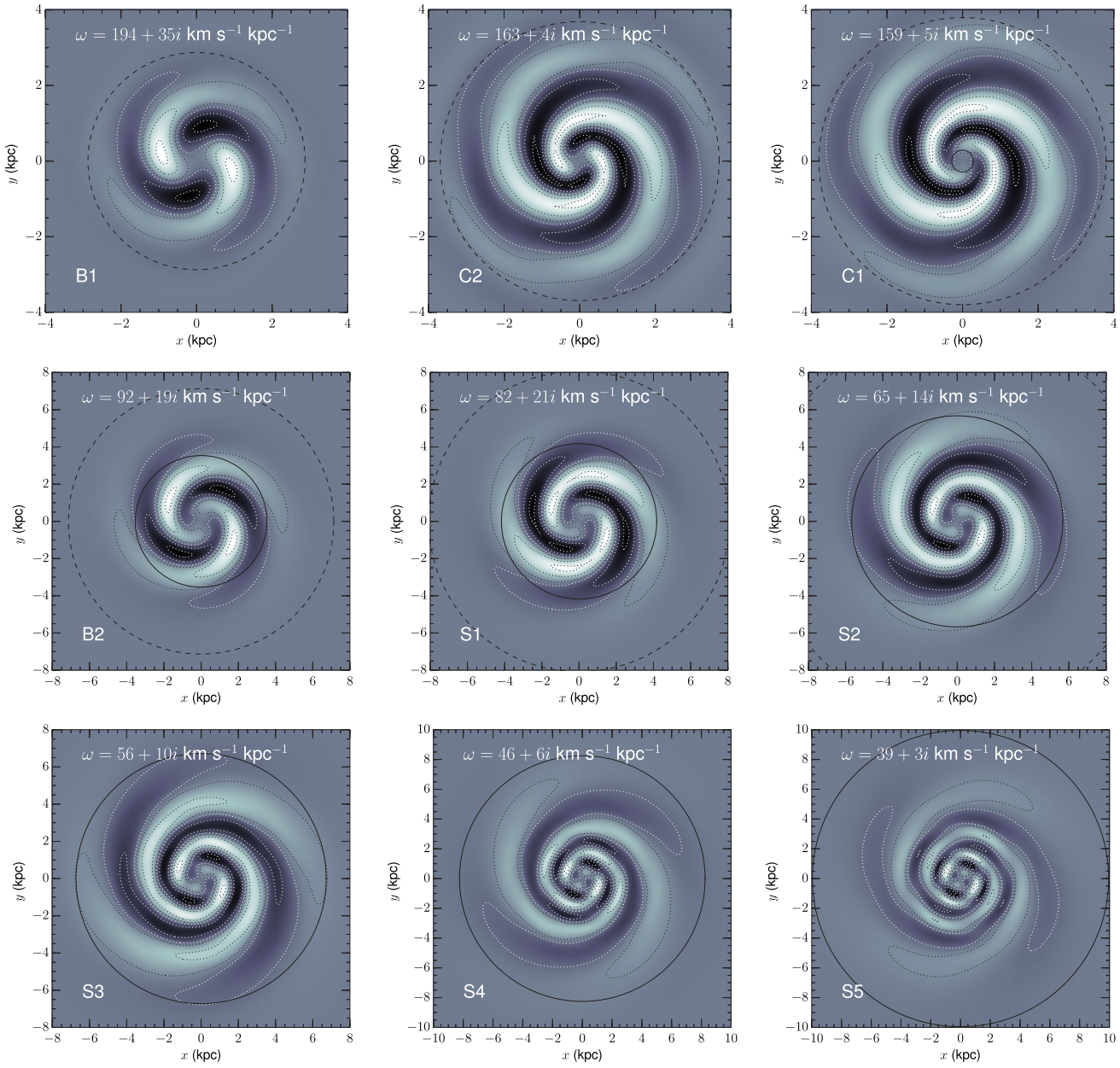

Figure 5. Surface density of the most prominent $m = 2$ eigenmodes of the cored exponential disc model, labelled by their complex frequency ω and their name taken from Jalali (2007). Positive densities are drawn in light-greys/white; negative ones in dark-greys/black. The corotation radius is indicated with a thick full line; the outer Lindblad resonance by a dashed line. The thin dotted line contours trace surface density levels at ±10, ±50 and ±90 per cent of the maximum value.

from a narrow strip around a fixed angular momentum $J_{\rm groove}$ by multiplying the original DF, given by equation (23), with a function $H_{\rm groove}(J)$ of the form

$$H_{\rm groove}(J) = 1 - e^{-\frac{x^6}{\sigma_1}} + Ae^{-\frac{(x-1.5)^2}{\sigma_2}} \tag{28}$$

with $x = (J - J_{\rm groove})/w_J$. Here, we choose $w_J = 60$ kpc km s^{-1}, $\sigma_1 = 2.0, \sigma_2 = 0.5$ and the forefactor A such that the narrow positive bump cancels the broader negative groove. In other words: stars are removed from the groove and deposited at the groove's high-J edge. As an example, the top panel of Fig. 7 shows the DF of the model with a groove centred on $J_{\rm groove} = 433$ kpc km s^{-1}. This is reflected in a narrow, curved groove in the DF in turning-point space ending in the circular orbit with radius $r_{\rm circle} = 2.87$ kpc.

Since the ridge at the edge of the DF groove to a good approximation conserves the number of stars, the epicyclic motions of the stars cause the groove to have only a minor effect on the stellar surface density. Only around the radius of the circular orbit with angular momentum equal to $J_{\rm groove}$ is there a small wiggle in the density, as can be seen in Fig. 7. Likewise, the radial velocity dispersion remains virtually unaffected. The groove increases the Toomre Q-parameter (Toomre 1964) by approximately 15 per cent around the groove radius. The mean tangential velocity and, specifically, the tangential velocity dispersion are significantly affected by the groove. Since stars on circular orbits inside the groove have been

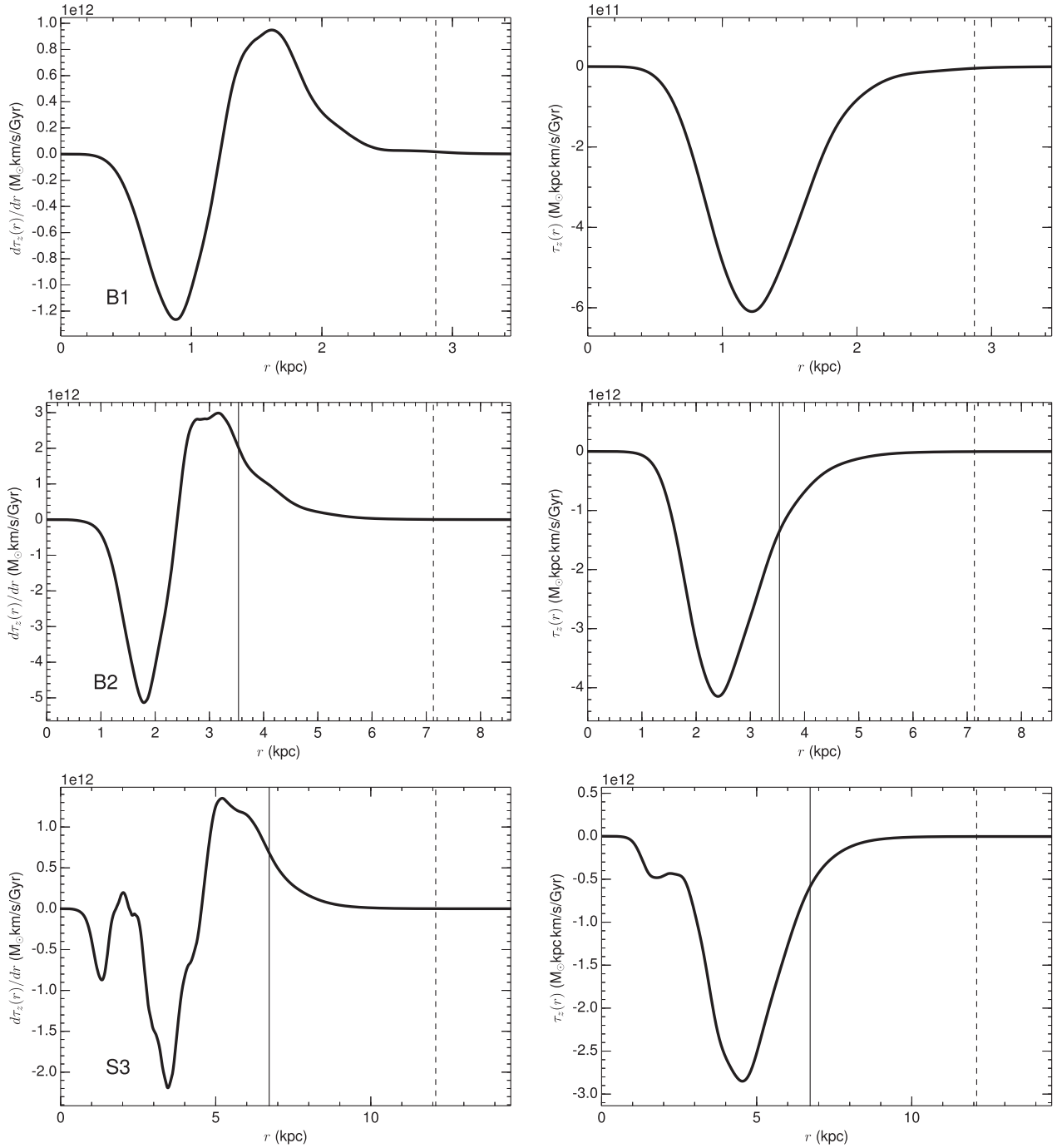

Figure 6. Left column: the torque $d\tau_z(r)$ exerted by the spiral pattern on an annular ring of stars with radius r and width dr. Right column: the torque $\tau_z(r)$ integrated out to radius r. Top to bottom: the eigenmodes B1, B2 and S3 of the cored exponential disc model. Vertical full line: the CR radius; vertical dashed line: the OLR radius.

removed from the DF, it is mostly stars on eccentric orbits that venture from the groove's high-J bump towards the groove, thus locally increasing the tangential velocity dispersion. Their epicyclic motions locally contribute to the tangential velocity, leading to an increase of the rotation velocity at the groove radius. The removal of stars on eccentric orbits that move outside of the gap (see Fig. 7) explains the drop of the dispersion at the edges of the groove.

In Fig. 8, the mode spectra of several cored exponential disc models with different narrow phase space grooves, centred on the angular momentum $J_{\rm groove}$ indicated in each panel, are shown in the complex frequency plane. These grooved models are listed in Table 2. From left to right and from top to bottom in Fig. 8, the angular momentum $J_{\rm groove}$ of the groove increases while the corotation frequency $\omega_{\rm groove}$ decreases. The white hatched region in each panel, centred on the frequency $\omega_{\rm groove}$, indicates the locus of the modes that corotate with stars on circular orbits inside the groove. The coloured triangles indicate the position of the growing eigenmodes of the original cored exponential disc model, as listed in Table 1. For any choice of $J_{\rm groove}$, there are modes present that grow faster than in the ungrooved model. Only for very high $J_{\rm groove}$-values

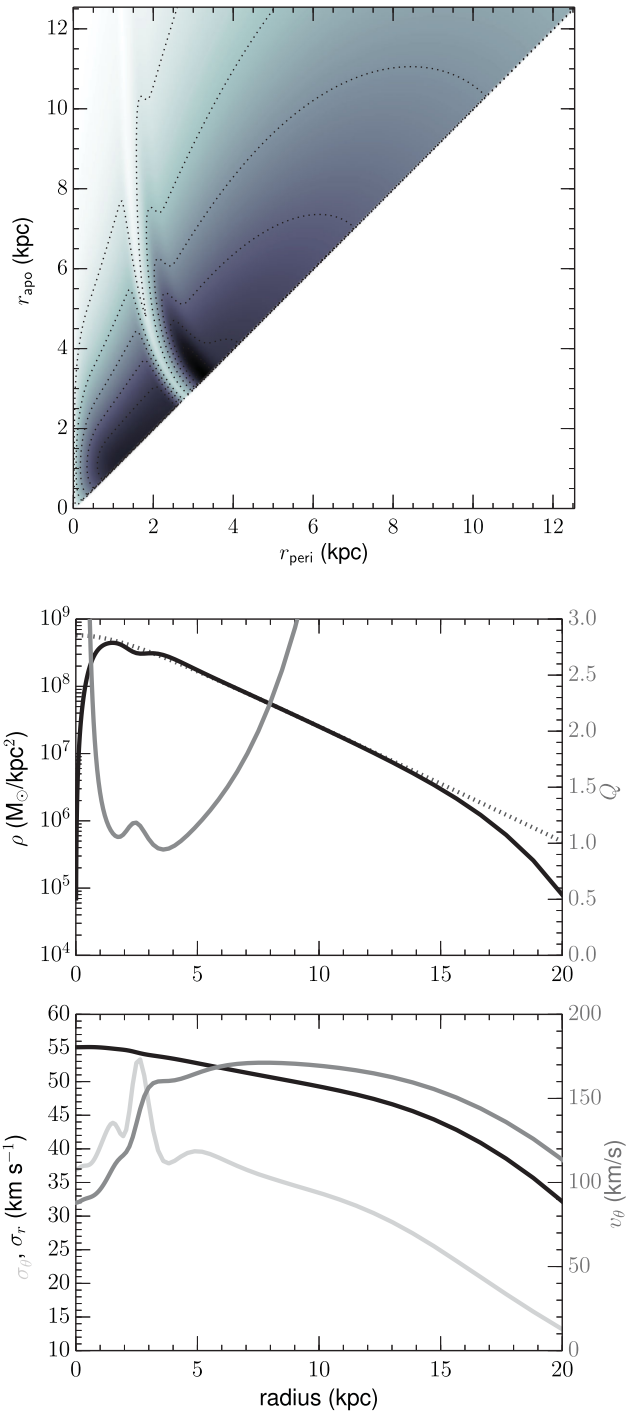

Figure 7. Top panel: the distribution function of the cored exponential disc model with a central cutout and with a groove at $J_{\rm groove} = 433$ kpc km s^{-1}, shown in turning-point space. The colour bar indicates the phase-space density expressed in $M_\odot$ kpc^{-2} (km s^{-1})$^{-2}$. Middle panel: the stellar density, ρ (black curve, left axis) and the Toomre Q-parameter (dark grey curve, right axis). The dotted black curve traces the stellar density (22), without inner cutout and outer tapering. Bottom panel: the radial velocity dispersion, σ_r (black curve, left axis), tangential velocity dispersion, σ_θ (light grey curve, left axis) and the mean rotation velocity, v_θ (dark grey curve, right axis) of the cored exponential disc model with an inner cutout and with a groove at angular momentum $J_{\rm groove} = 433$ kpc km s^{-1}, corresponding to a circular orbit with radius 2.87 kpc, the OLR of mode B1.

does the grooved model's eigenmode spectrum approach that of the ungrooved model.

A groove in phase space clearly can have an impressive and destabilizing effect on the eigenmode spectrum of a disc galaxy model, dramatically affecting the number and the frequencies of the modes. Below, we discuss the modes associated with the groove in more detail.

4.1 High and low frequency modes

The grooved exponential disc supports couples of modes that straddle the groove in frequency space. In other words: these modes have corotation radii either inside (the so-called 'high-frequency' modes) or outside (the so-called 'low-frequency' modes) the groove. Their density distributions are shown in Figs 9 and 10. Moreover, the two modes of each couple have virtually identical growth rates, given by $\omega_{\rm imag}$, and will co-evolve to non-linearity. Remarkably, the OLR of the fastest rotating mode often lies very close to the CR of the slowest rotating mode. Given this close resonance proximity, they are likely to interact with each other, producing $m = 0$ and $m = 4$ beat waves (Sygnet et al. 1988; Masset & Tagger 1997).

Especially for grooves at small angular momentum, in this case this is for $J_{\rm groove} \lesssim 400$ kpc km s^{-1}, these are the fastest growing members of the grooved disc's eigenmode spectrum. There are no $m = 2$ modes in the ungrooved exponential disc that could carve a groove at these small $J_{\rm groove}$-values although the fastest rotating $m = 4$ mode we found (cf. Section 5) has its OLR at 2.36 kpc, which corresponds to a groove angular momentum of $J_{\rm groove} = 323$ kpc km s^{-1}. For higher $J_{\rm groove}$-values, these modes shift gradually towards lower pattern speeds and smaller growth rates and, finally, they disappear among the modes of the ungrooved model.

The low-frequency modes have a radial node at the groove's outer edge while the high-frequency modes have a radial node at the groove's inner edge (although the strength of the part of the mode outside the groove diminishes with increasing $J_{\rm groove}$). This is likely to be a strong clue regarding the origin of these modes as standing wave patterns formed by travelling waves reflecting off the groove's inner and outer edge.

4.2 Medium frequency mode

Around $J_{\rm groove} \approx 200$ kpc km s^{-1}, a 'medium-frequency' mode is destabilized with a frequency in between that of the high- and low-frequency modes. It sits just at the low-frequency side of the groove in frequency space (see Fig. 8). Hence, the mode's CR radius sits just outside the groove (see Fig. 11). Although absent for the very lowest $J_{\rm groove}$-values, it overtakes the high- and low-frequency modes in growth rate around $J_{\rm groove} \sim 400$ kpc km s^{-1}. While the eigenmode spectrum approaches that of the ungrooved model for very high $J_{\rm groove}$-values, this 'medium-frequency' mode stays present. As can be seen in Fig. 11, the density distribution of a 'medium-frequency' mode never strays significantly beyond the groove's inner edge. This suggests that the 'medium-frequency' mode is a standing wave pattern formed by waves travelling between the galaxy centre and the groove's inner edge. The density distributions presented in Fig. 11 can be compared with fig. 7 in Sellwood & Kahn (1991). In the latter, the density distribution of a $m = 2$ mode in an N-body simulation of a grooved Mestel disc model is shown. Its CR radius lies just outside of the groove and its density is only significantly non-zero inside the groove or, equivalently, its CR radius. In other words, it looks exactly as one would expect of a 'medium-frequency' mode.

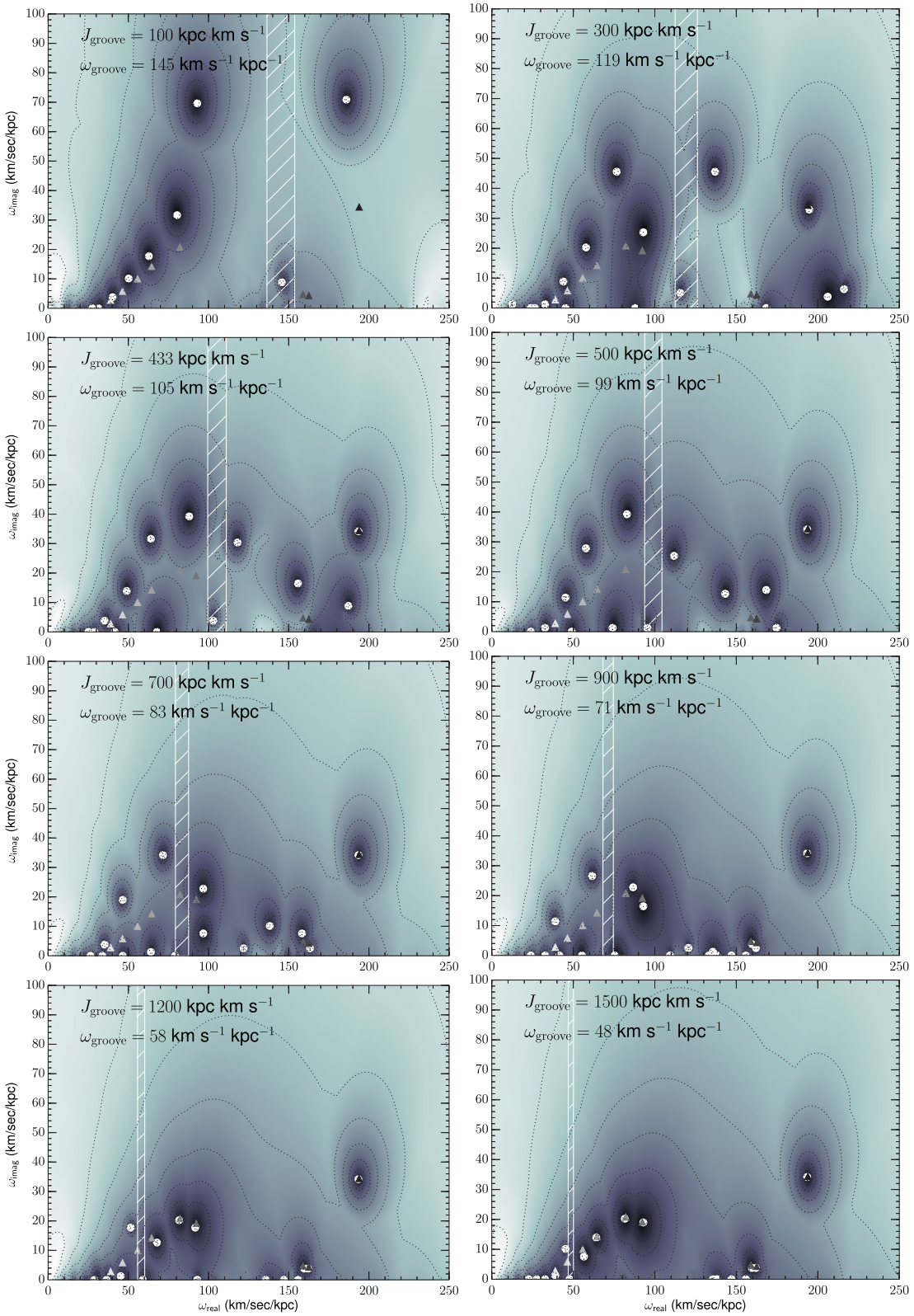

Figure 8. The $m = 2$ mode spectrum in the complex frequency plane of cored exponential disc models with different narrow phase space grooves, centred on the angular momentum $J_{\rm groove}$ indicated in each panel. The white hatched region in each panel, centred on the frequency $\omega_{\rm groove}$, indicates the locus of the modes that corotate with stars on circular orbits inside the groove. The coloured triangles indicate the position of the $m = 2$ eigenmodes of the original cored exponential disc model, as listed in Table 1.

Table 2. Models with a groove around angular momentum $J_{\rm groove}$. $r_{\rm circle}$ is the radius of the circular orbit with angular momentum $J_{\rm groove}$. $\omega_{\rm groove}$ is the frequency of a mode with corotation at $r_{\rm circle}$.

$J_{\rm groove}$ (kpc km s^{-1})	$\omega_{\rm groove}$ (km s^{-1} kpc^{-1})	$r_{\rm circle}$ (kpc)
100	144.8	1.18
200	131.2	1.75
300	119.0	2.25
433	105.1	2.87
500	98.9	3.18
600	90.6	3.64
700	93.3	4.10
800	76.9	4.56
900	71.3	5.03
1200	57.9	6.44
1500	48.4	7.87

In contrast to the modes in the ungrooved disc, the torque $\mathrm{d}\tau_z(r)$ exerted by the spiral pattern on the stellar disc can show a complex radial dependence, with several sign changes. These are caused by the sudden changes in the pattern's density and potential connected with the groove. Still, the total torque $\tau_z = \int_0^\infty \mathrm{d}\tau_z(r)$ is zero to a very good precision (see Fig. 12).

4.3 Groove mode

The grooves with $J_{\rm groove} \lesssim 600$ kpc km s^{-1} destabilize a mode with its CR radius squarely within the groove. This so-called 'groove'-mode grows much more slowly than the low-, medium- and high-frequency modes and is therefore dynamically less important. As is obvious from Fig. 13, this mode shows a tightly-wound *leading* spiral pattern inside the groove edge and a *trailing* spiral pattern

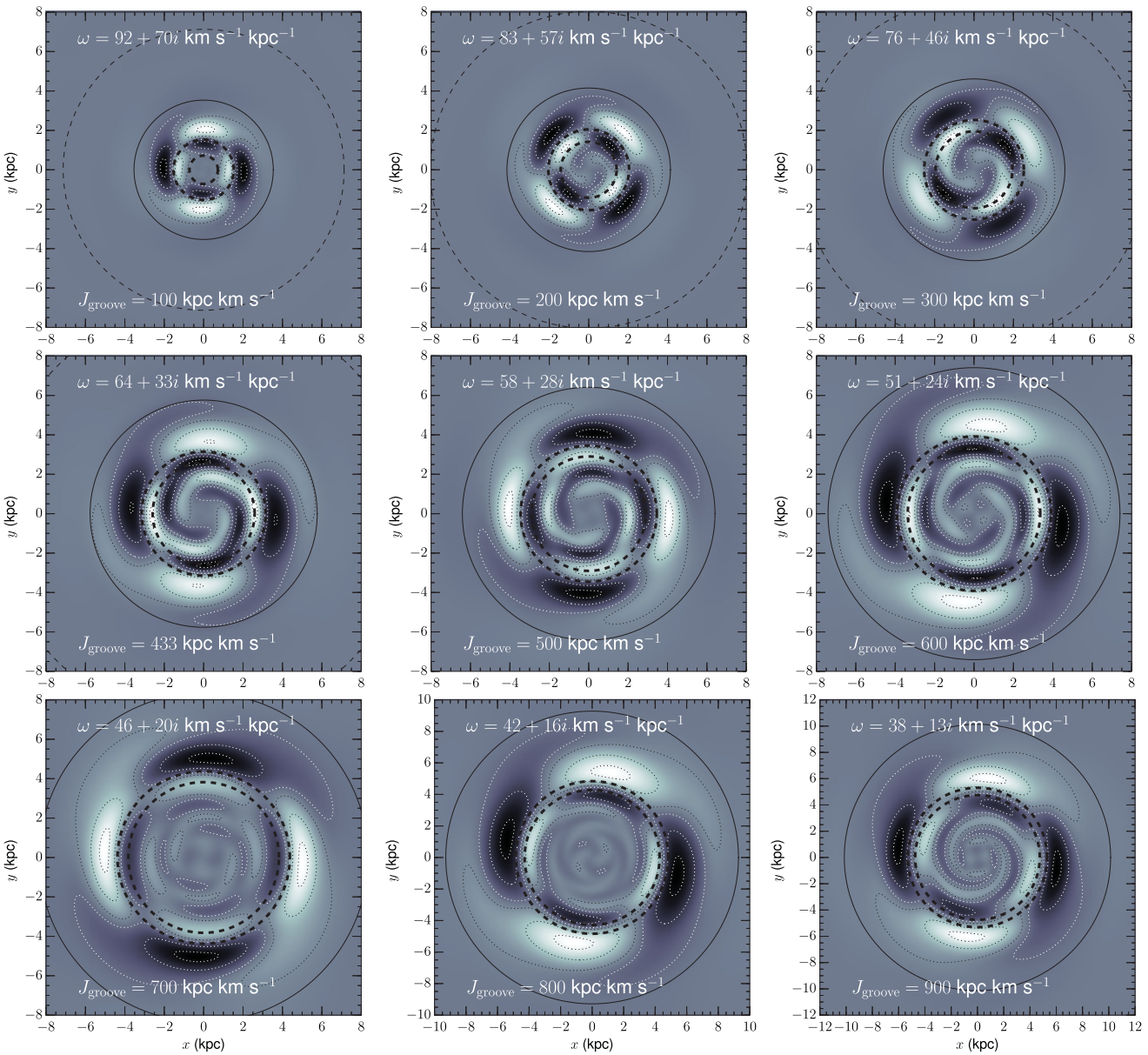

Figure 9. Surface density of the $m = 2$ 'low-frequency' modes in the cored exponential disc model with a groove at $J_{\rm groove}$ as indicated in each panel. Each panel is labelled with the complex frequency ω of the mode in question. The groove edges are indicated in thick dashed lines, the corotation radius in a thin full line and the outer Lindblad resonance in a thin dashed line.

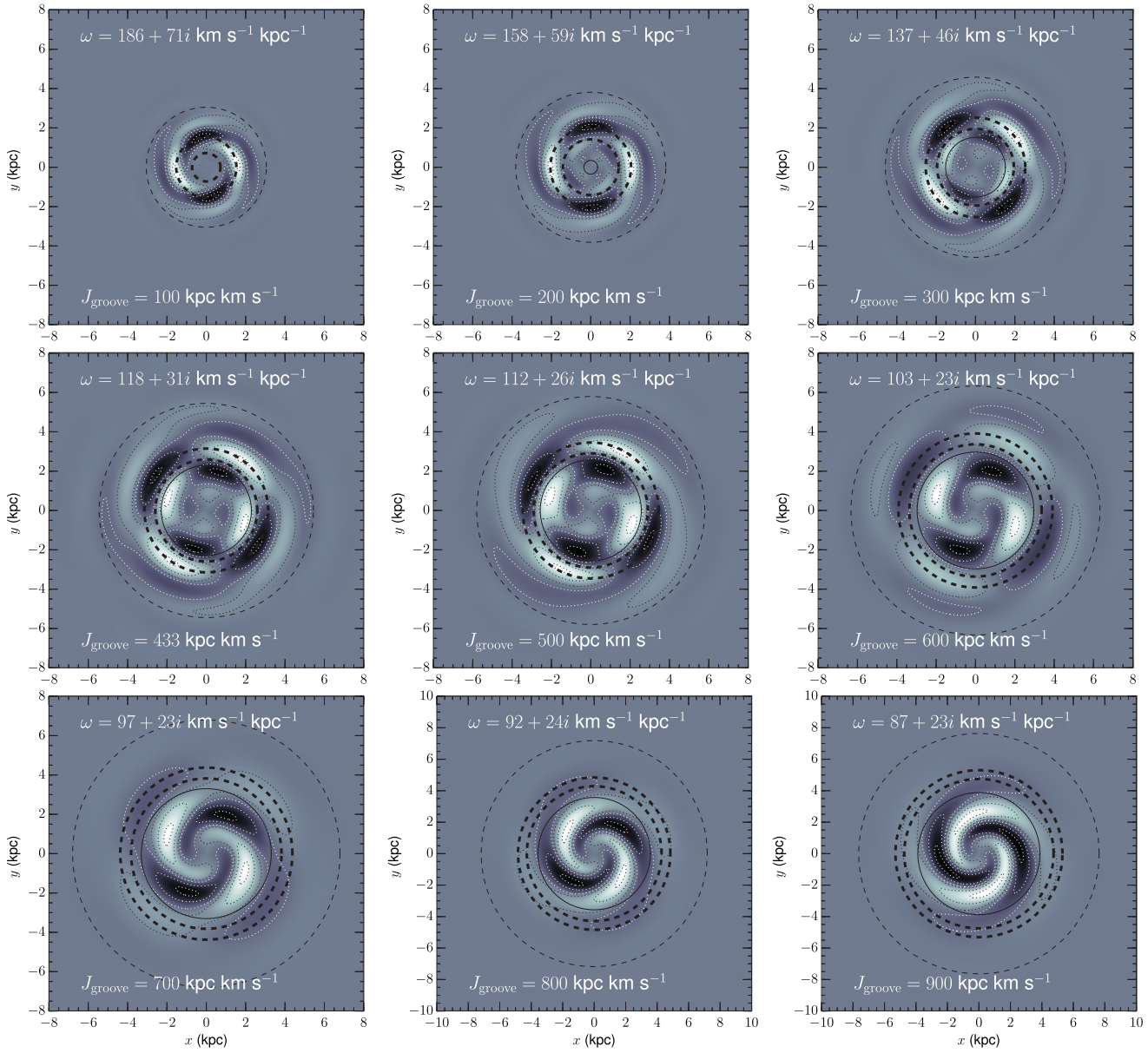

Figure 10. Surface density of the $m = 2$ 'high-frequency' modes in the cored exponential disc model with a groove at $J_{\rm groove}$ as indicated in each panel. Each panel is labelled with the complex frequency ω of the mode in question. The groove edges are indicated in thick dashed lines, the corotation radius in a thin full line and the outer Lindblad resonance in a thin dashed line.

beyond the groove. Apparently, travelling tightly wound leading waves dominate trailing waves in setting up these very slowly growing spiral patterns.

As the strength of the part of the mode outside the groove's outer edge diminishes with increasing $J_{\rm groove}$, the mode's central part eventually changes from a leading into a trailing spiral.

5 GROOVES AND *m*=4 MODES

In the top-left panel of Fig. 14, we show the $m = 4$ mode spectrum of the ungrooved exponential disc model in the complex frequency plane. It closely matches that presented in Jalali (2007) but since the latter was computed for an exponential disc without a central hole we will not attempt a quantitative comparison. The density distributions of three eigenmodes are presented in Fig. 15. The fastest rotating modes, with $\omega_{\rm real} \gtrsim 300$ km s^{-1} kpc^{-1}, lack a CR and are confined within their OLR radius. The leftmost mode in Fig. 15 serves as an example. The second series of modes, between $\omega_{\rm real} \sim 160$ km s^{-1} kpc^{-1} and $\omega_{\rm real} \sim 240$ km s^{-1} kpc^{-1}, comprises modes that rotate sufficiently slowly to have a CR but fast enough to avoid having an ILR. Their growth rate drops to zero for modes close to having an ILR. The mode shown in the middle panel of Fig. 15 belongs to this series. The modes with frequencies between $\omega_{\rm real} \sim 100$ km s^{-1} kpc^{-1} and $\omega_{\rm real} \sim 150$ km s^{-1} kpc^{-1} all have an ILR and have a density distribution that exists mainly between the ILR and the CR radius, cf. the right-hand panel of Fig. 15.

The fastest rotating $m = 4$ mode has an OLR radius of 2.36 kpc and, while it is far from being a strong mode, it could be capable of carving a groove in a very reactive region of the phase space of this disc galaxy model (see Section 4), making it potentially crucial for

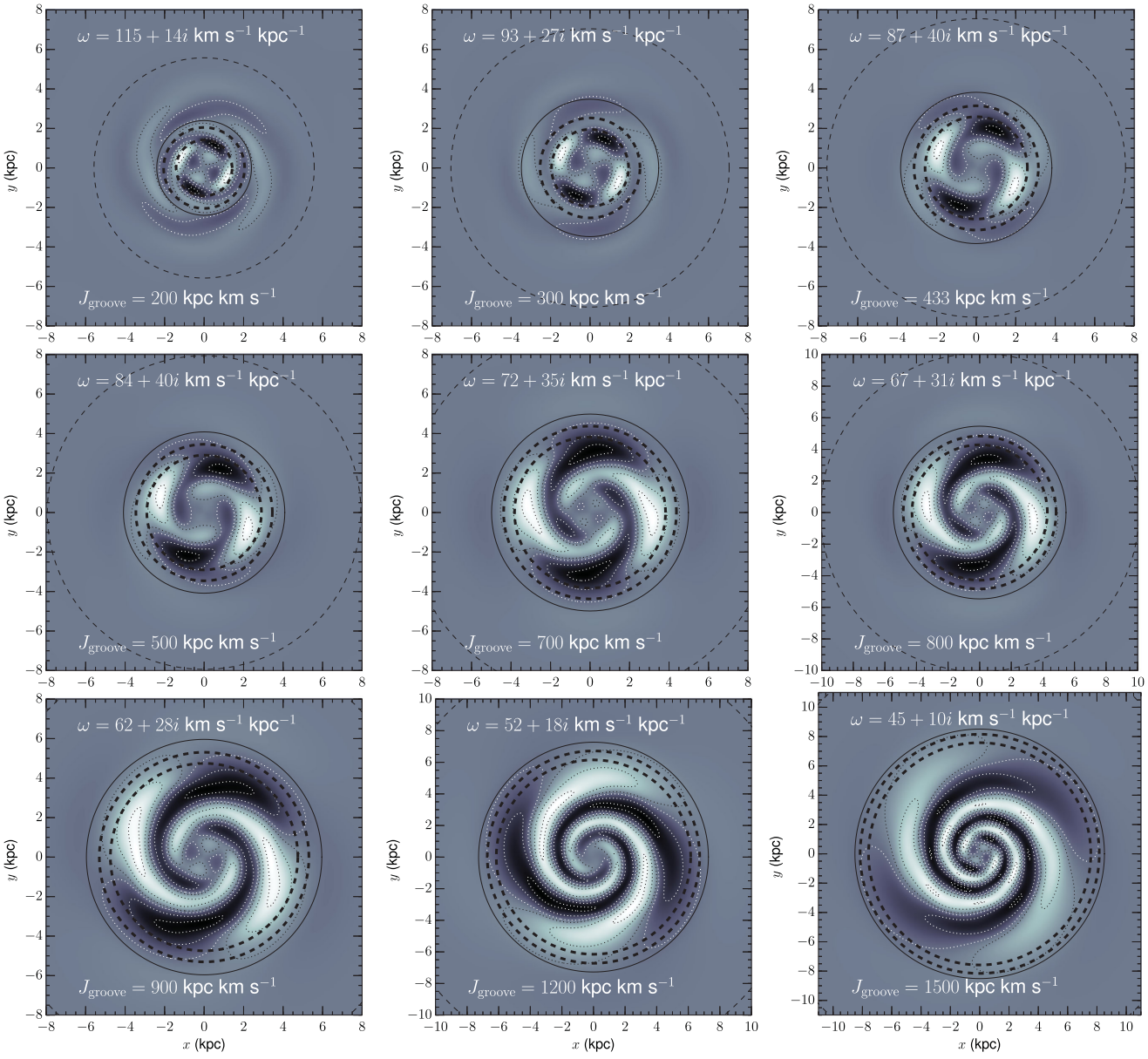

Figure 11. Surface density of the $m = 2$ 'medium-frequency' modes in the cored exponential disc model with a groove at $J_{\rm groove}$, as indicated in each panel. Each panel is labelled with the complex frequency ω of the mode in question. The groove edges are indicated in thick dashed lines, the corotation radius in a thin full line and the outer Lindblad resonance in a thin dashed line.

the existence of the second generation of $m = 2$ eigenmodes in this disc galaxy model.

As was the case for the two-armed modes, a groove has a very destabilizing effect on the four-armed patterns as evidenced by the eigenmode spectra shown in Fig. 14. For $J_{\rm groove} \lesssim 300$ kpc km s^{-1}, the $m = 4$ eigenmode spectrum is dominated by two modes which are the analogs of the 'high-frequency' and 'low-frequency' modes we encountered in the $m = 2$ spectra. As $J_{\rm groove}$ is increased, a 'medium-frequency' mode quickly gains strength and overtakes the 'high-frequency' and 'low-frequency' modes. Its frequency shifts upwards with increasing $J_{\rm groove}$ until, for $J_{\rm groove} \gtrsim 300$ kpc km s^{-1}, it sits firmly within the groove. For still higher, $J_{\rm groove}$ values, the $m = 4$ eigenmode spectrum is dominated by a 'low-frequency' and a 'medium-frequency/groove' mode.

In Fig. 16, we show the density distributions of the $m = 4$ low-frequency mode (left-hand panel), the medium-frequency mode (middle panel) and the high-frequency mode (right-hand panel) for the cored exponential disc model with a groove at $J_{\rm groove} = 300$ kpc km s^{-1}. These show the same radial behaviour as their two-armed analogs. The medium-frequency modes are limited to the disc region inside the groove's inner edge while the low-frequency and high-frequency modes have radial nodes at the groove's outer and inner edge, respectively. Given this morphological similarity between the two- and four-armed modes, their origin, in terms of wave dynamics, is most likely also similar.

Using *N*-body simulations, Sellwood & Lin (1989) found the dominant four-armed mode to have a CR radius coincident with the groove and to be accompanied by a small number of other

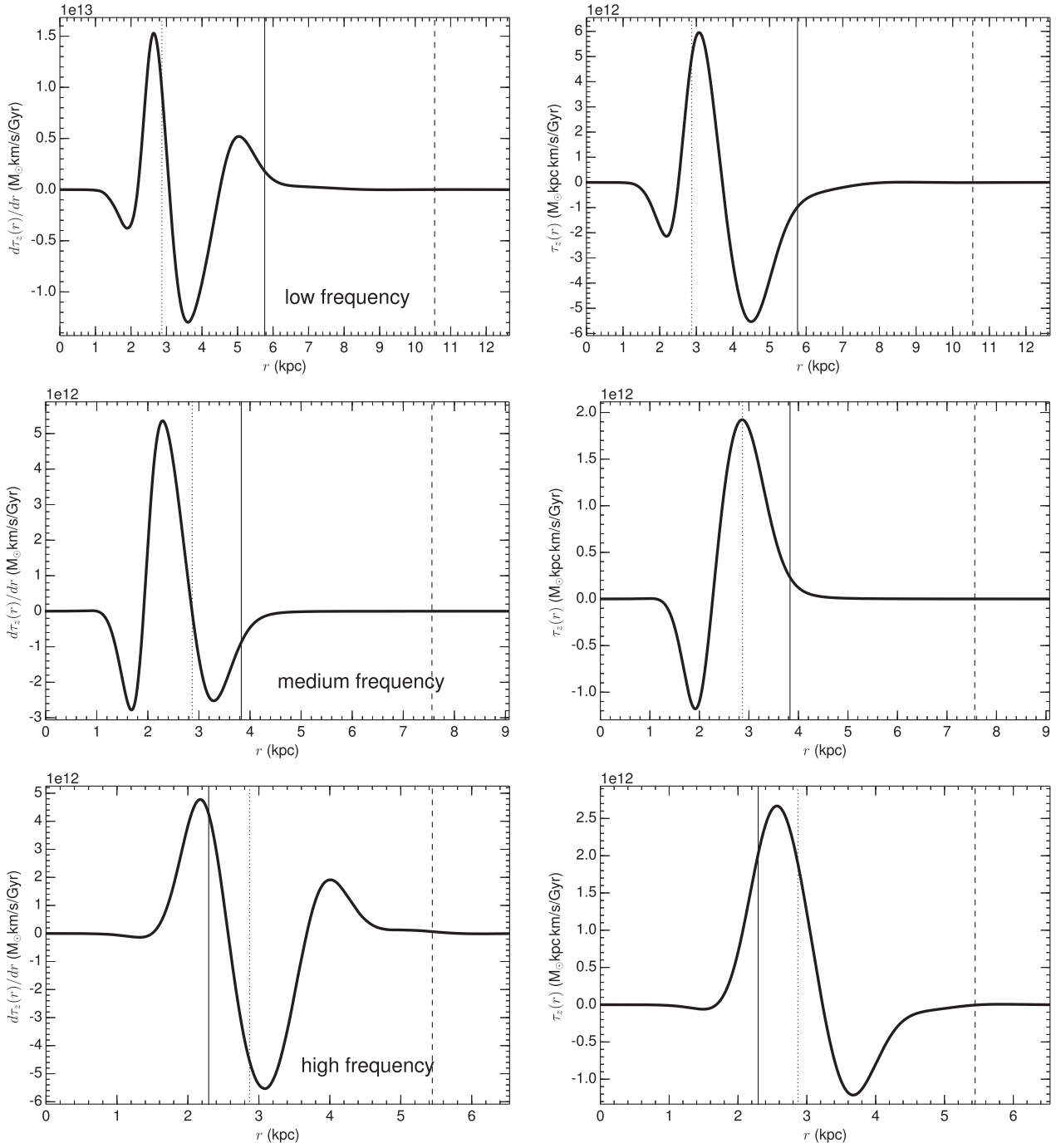

Figure 12. Left column: the torque $\mathrm{d}\tau_z(r)$ exerted by the spiral pattern on an annular ring of stars with radius r and width $\mathrm{d}r$. Right column: the torque $\tau_z(r)$ integrated out to radius r. Top to bottom: the low-frequency, medium-frequency and high-frequency eigenmodes of the cored exponential disc model with a groove at $J_{\mathrm{groove}} = 433$ kpc km s^{-1}. Vertical full line: the CR radius; vertical dashed line: the OLR radius.

modes. These observations are in qualitative agreement with ours for a groove in the intermediate J_{groove}-range, where the medium-frequency mode dominates.

6 GROOVE SHAPE

We investigated how the shape of the groove affects the mode spectrum by calculating the latter, on the one hand, for a $J_{\mathrm{groove}} = 433$ kpc km s^{-1} groove with no high-J ridge and, on the other hand, for the same groove but with both a compensating low-J and a high-J ridge. Evidently, a groove without ridges does not conserve the total stellar mass and therefore has a visible impact on the model's velocity moments. To be specific: it significantly increases Toomre's Q around the groove radius. The groove with two ridges does conserve stellar mass and, consequently, has a much weaker effect on the kinematics.

As can be seen in Fig. 17, the presence or absence of ridges has a strong effect on the mode spectrum. A groove without ridges

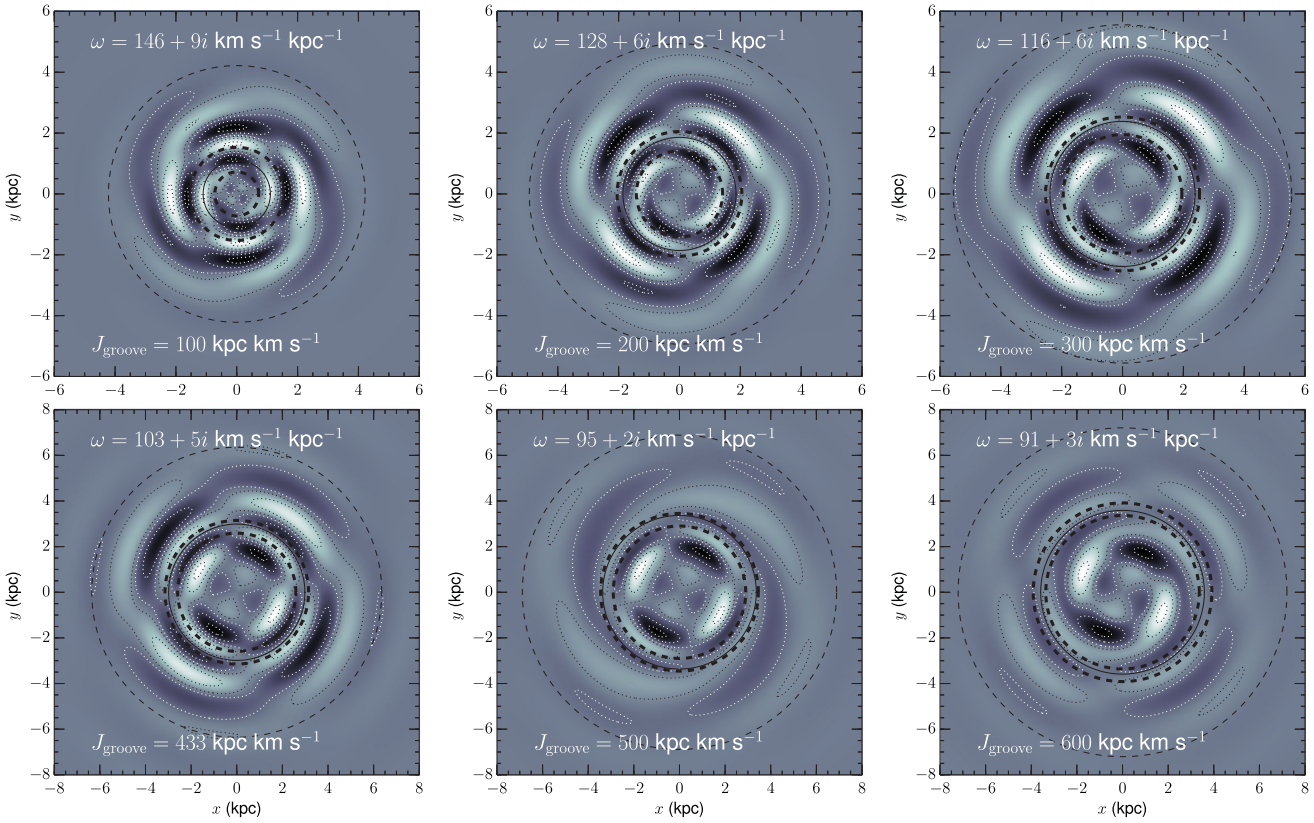

Figure 13. Surface density of the $m = 2$ 'groove' modes in the cored exponential disc model with a groove at $J_{\rm groove}$, as indicated in each panel. Each panel is labelled with the complex frequency ω of the mode in question. The groove edges are indicated in thick dashed lines, the corotation radius in a thin full line and the outer Lindblad resonance in a thin dashed line.

produces a strong medium-frequency mode but there is no low-frequency mode and the high-frequency mode is very weak. A groove with two ridges produces both the medium-frequency and a strong high-frequency mode but not the low-frequency mode. From this experiment, one can conclude that the existence of the medium-frequency mode only depends on the presence of the groove and *not* on the presence of the ridges. The ridges do affect the interference patterns producing the low- and high-frequency modes.

We also experimented with a groove at $J_{\rm groove} = 433$ kpc km s^{-1} with one compensating ridge but with half the width ($w_J = 30$ kpc km s^{-1}) as was used thus far. The eigenmode spectrum of this model is shown in the right-hand panel of Fig. 17 and can be directly compared with the corresponding panel of Fig. 8. The spectra look very much alike except for the fact that the modes associated with the narrower groove have slightly lower growth rates. The growth rate of the high-frequency mode seems particularly diminished. Therefore, within the range of groove widths investigated here, the width of the groove does not seem to significantly affect the position of the modes although it does influence their exponentiation timescales.

7 CONCLUSIONS

Using PYSTAB, a linear mode analysis computer code, we have computed the $m = 2$ and $m = 4$ eigenmode spectra of a cored razor-thin exponential disc galaxy model embedded in a logarithmic potential, as introduced by Jalali & Hunter (2005) and found excellent agreement with previous authors (Jalali & Hunter 2005; Jalali 2007; Omurkanov & Polyachenko 2014).

We investigated how a phase-space groove at a fixed angular momentum affects these eigenmode spectra. Our main conclusion is that a groove has an impressive impact on the linear stability properties of a disc galaxy. Depending on where in phase space the groove is carved, completely new eigenmodes come into existence. We have shown that the fastest rotating $m = 2$ and $m = 4$ modes of the ungrooved exponential disc model have OLR radii in a very responsive part of the disc's phase space and, if grooves are carved there, they would generate vigorously growing new eigenmodes.

Using the spatial density distribution of these modes, we have attempted to shed some light on their origin in terms of interference patterns of travelling waves. The intermediate-frequency modes are interference patterns that arise between the galaxy centre and the inner edge of the groove. The low- and high-frequency modes appear to have a radial node anchored to the groove's outer and inner edge, respectively. The very slowly growing modes with a CR radius coincident with the groove have complex density distributions, sometimes even with a partially leading spiral shape. These modes may be related to the spiral instabilities discussed in Polyachenko (2004). There, the author shows that if phase-space regions exist where the so-called Lynden–Bell derivative of the DF (a constrained angular-momentum derivative) is negative, unstable spiral modes are triggered. A narrow phase-space groove may be just such a region.

Thus, we confirm the hypothesis made by previous authors (Sellwood & Lin 1989; Sellwood & Kahn 1991) that spiral patterns beget new spiral patterns by carving grooves in phase space at successively larger radii. Because we are using first-order

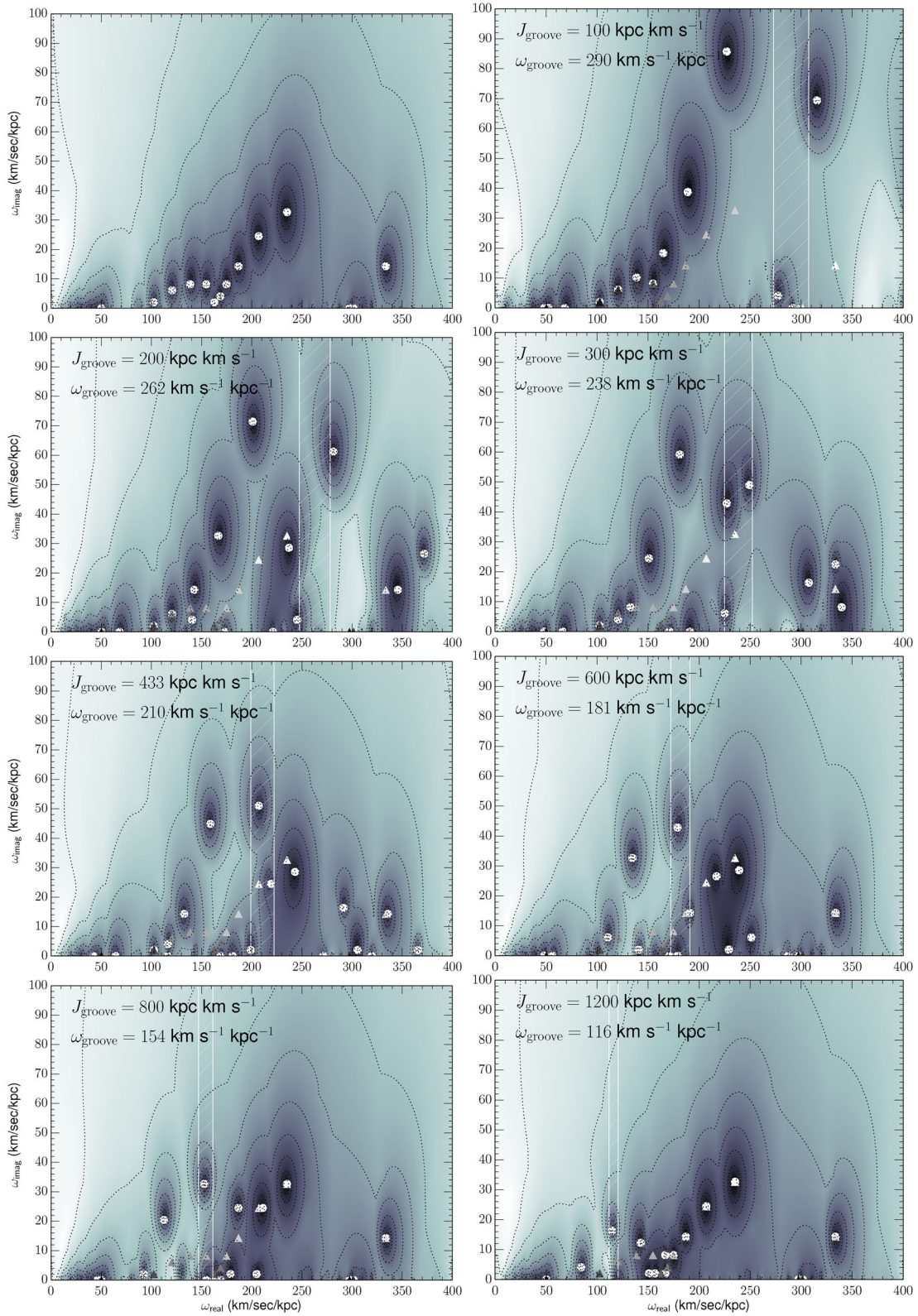

Figure 14. The $m = 4$ mode spectrum in the complex frequency plane of cored exponential disc models without a phase-space groove (top-left panel) and with different narrow phase space grooves, centred on the angular momentum $J_{\rm groove}$ indicated in each panel. The white hatched region in each panel, centred on the frequency $\omega_{\rm groove}$, indicates the locus of the modes that corotate with stars on circular orbits inside the groove. The coloured triangles indicate the position of the $m = 4$ eigenmodes of the original cored exponential disc model.

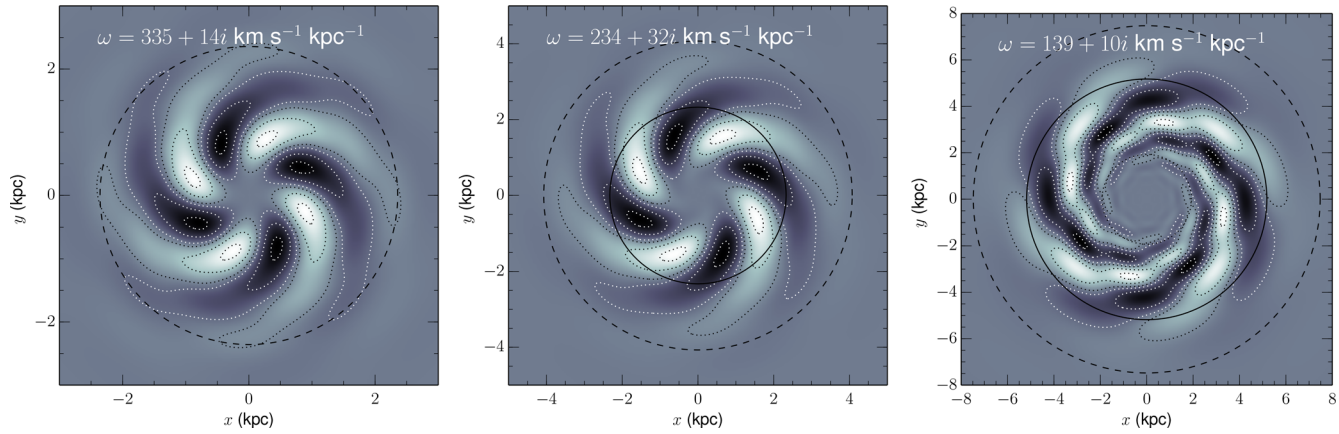

Figure 15. Surface density of the most prominent $m = 4$ eigenmodes of the ungrooved cored exponential disc model, labelled by their complex frequency ω. The corotation radius is indicated in a thin full line and the outer Lindblad resonance in a thin dashed line.

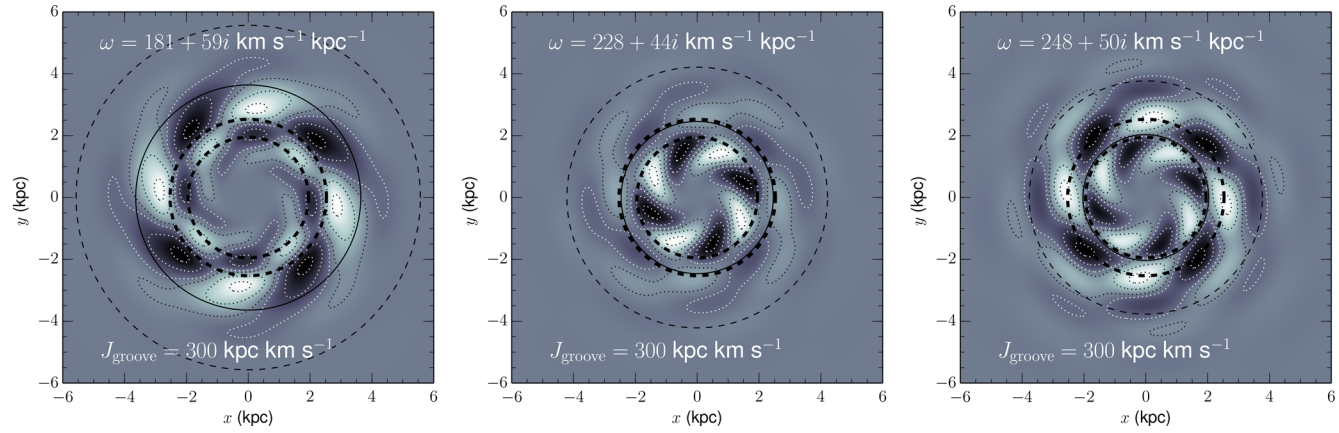

Figure 16. Surface density of the most prominent $m = 4$ eigenmodes of the cored exponential disc model with a groove at $J_{\rm groove} = 300$ kpc km s^{-1}, labelled by their complex frequency ω. The groove edges are indicated in thick dashed lines, the corotation radius in a thin full line and the outer Lindblad resonance in a thin dashed line.

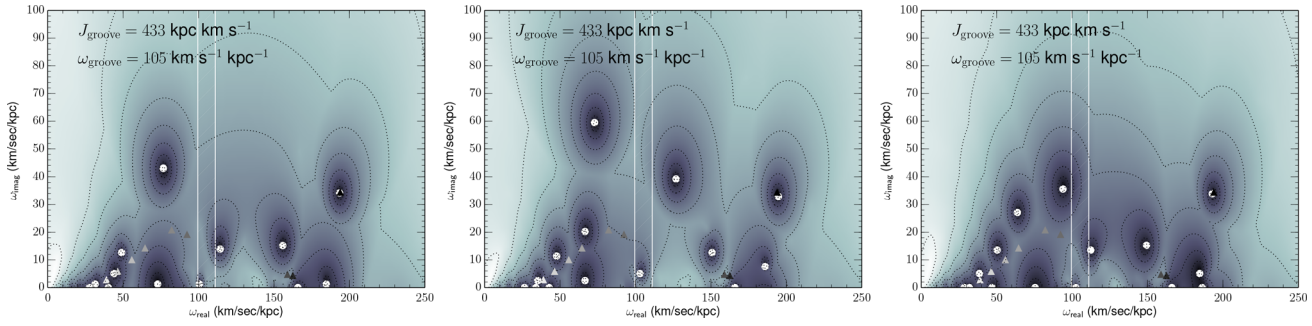

Figure 17. The $m = 2$ mode spectrum in the complex frequency plane of cored exponential disc models with a phase-space groove at $J_{\rm groove} = 433$ kpc km s^{-1}. Left-hand panel: a groove without compensating ridges. Middle panel: a groove with two compensating ridges. Right-hand panel: a groove with one compensating ridge but half the width ($w_J = 30$ kpc km s^{-1}). The white hatched region in each panel, centred on the frequency $\omega_{\rm groove}$, indicates the locus of the modes that corotate with stars on circular orbits inside the groove. The coloured triangles indicate the position of the $m = 2$ eigenmodes of the original cored exponential disc model.

perturbation theory to construct and compare the eigenmode spectra of grooved and ungrooved models, we can rule out two of the possible origins of the wave patterns observed in simulated grooved disc galaxies as suggested by Sellwood & Lin (1989): these patterns are not intrinsic modes of the original, ungrooved disc and they are not due to non-linear mode coupling. We do confirm the third possibility raised by these authors: they are true eigenmodes, particular to the grooved disc.

ACKNOWLEDGEMENTS

The authors wish to thank V. P. Debattista (UCLAN, UK) for his helpful comments on an earlier draft of this manuscript. We also thank our anonymous referee for his/her helpful remarks.

REFERENCES

D'Onghia E., Vogelsberger M., Hernquist L., 2013, ApJ, 766, 34
Dury V., de Rijcke S., Debattista V. P., Dejonghe H., 2008, MNRAS, 387, 2
Goldreich P., Lynden-Bell D., 1965, MNRAS, 130, 125
Jalali M. A., 2007, ApJ, 669, 218
Jalali M. A., 2010, MNRAS, 404, 1519
Jalali M. A., Hunter C., 2005, ApJ, 630, 804
Julian W. H., Toomre A., 1966, ApJ, 146, 810
Kalnajs A. J., 1977, ApJ, 212, 637
Lin C. C., Shu F. H., 1964, ApJ, 140, 646
Lynden-Bell D., Kalnajs A. J., 1972, MNRAS, 157, 1
Mark J. W.-K., 1977, ApJ, 212, 645
Masset F., Tagger M., 1997, A&A, 322, 442
Omurkanov T. Z., Polyachenko E. V., 2014, Astron. Lett., 40, 724
Polyachenko E. V., 2004, MNRAS, 348, 345
Polyachenko E. V., 2005, MNRAS, 357, 559
Polyachenko E. V., Just A., 2015, MNRAS, 446, 1203
Sanderson S., 2010, Technical Report, NICTA
Sellwood J. A., Kahn F. D., 1991, MNRAS, 250, 278
Sellwood J. A., Lin D. N. C., 1989, MNRAS, 240, 991
Sygnet J. F., Tagger M., Athanassoula E., Pellat R., 1988, MNRAS, 232, 733
Toomre A., 1964, ApJ, 139, 1217
Toomre A., 1981, in Fall S. M., Lynden-Bell D., eds, Structure and Evolution of Normal Galaxies, p. 111. Cambridge Univ. Press, Cambridge
Vauterin P., Dejonghe H., 1996, A&A, 313, 465
Zhang X., 1996, ApJ, 457, 125
Zhang X., 1998, ApJ, 499, 93

This paper has been typeset from a TEX/LATEX file prepared by the author.